

Cascaded degenerate four-wave mixing generation in thin-film lithium tantalate microdisk cavity


Xiongshuo Yan,^{1,†} Miao Xue,^{1,†} Tingge Yuan,¹ Jiangwei Wu,¹ Rui Ge,¹ Yuping Chen^{1,2,*} and Xianfeng Chen^{1,3,4}

¹*Shanghai Jiao Tong University, School of Physics and Astronomy, State Key Laboratory of Advanced Optical Communication Systems and Networks, Shanghai 200240, China*

²*Ningxia University, School of Physics, Yinchuan 750021, China*

³*Shandong Normal University, Collaborative Innovation Center of Light Manipulation and Applications, Jinan 250358, China*

⁴*Shanghai Research Center for Quantum Sciences, Shanghai 201315, China*

 (Received 1 August 2023; revised 8 October 2023; accepted 25 January 2024; published 16 February 2024)

On-chip efficient nonlinear functions are instrumental in escalating the utilities and performance of photonic integrated circuits, especially for a wide range of classical and quantum applications, such as tunable coherent radiation, optical frequency conversion, spectroscopy, quantum science, etc. Here, we fabricated a Z-cut lithium tantalate on insulator (LTOI) microdisk with high quality ($Q \sim 10^6$) factors. Cascaded three- and four-wave mixing generation simultaneously were achieved in the LTOI microdisk cavity, due to the high Q factor with a strongly confined light field, relatively large nonlinear coefficient, and optical damage threshold of the LTOI microdisk. The strict mode phase-matching condition and the second-harmonic efficiency of the whole three-wave mixing processes were analyzed. Our work shows that the LTOI microresonators with the high Q factor and its high optical damage threshold and wide transparency range can support a variety of on-chip optical nonlinear processes, which heralds its application potential in integrated nonlinear photonics.

DOI: [10.1103/PhysRevApplied.21.024033](https://doi.org/10.1103/PhysRevApplied.21.024033)

I. INTRODUCTION

On-chip efficient and compact frequency converters are promising to be one of the key components in the wavelength-division-multiplexing (WDM) systems and have a range of applications, such as tunable coherent radiation [1,2], telecommunications [3,4], spectroscopy, and quantum optics [5–8]. Nonlinear optics provides a convenient route to access the frequencies we are interested in. Since the nonlinear susceptibilities are very small [9] as $\chi^{(2)} \sim 10^{-12}$ m/V, $\chi^{(3)} \sim 10^{-24}$ m²/V², the nonlinear response of a material system can be obtained only when laser light is sufficiently intense and the material should better have large nonlinear susceptibilities. That means to achieve efficient nonlinear reactions, we should load the laser with enough intensity and choose these materials with large nonlinear susceptibilities. Optical whispering-gallery-mode (WGM) microcavities owing to their strong confinement of a light field (ultrahigh quality factors and small mode volumes) could considerably enhance the light-matter interaction [10], making it an ideal platform

for studying a broad range of nonlinear optical effects [11–14], ultrahigh sensitivity sensors [15,16], and other physical applications [17,18]. It should be noted that although the structure of optical WGM microcavities can enlarge the intracavity laser intensity, it also has to satisfy other criteria, such as phase matching, a large mode overlap among the interaction modes, and large nonlinear susceptibilities, etc., to obtain effective nonlinear processes [19,20].

Lithium niobate (LN), as one of the famous nonlinear materials, has large second-order nonlinear susceptibility and many other excellent physical properties, such as high refractive index, strong electro-optic, acousto-optic, and piezoelectric effects [21]. Many on-chip photonic devices such as quantum transducers, modulators, filters, etc., [22–25], and nonlinear processes (e.g., SHG, OPO, frequency combs, etc. [6,26–40]), based on LN have been developed. What is more, rare-earth ion-doped thin-film LN is achieved, and on-chip microcavity lasers and waveguide amplifiers are also investigated, although LN itself has no gain characteristics based on transitions between two electronic levels [41–48]. Nevertheless, LN has the advantage of a large nonlinear coefficient for nonlinear processes, there are some shortages for LN as low optical damage threshold (0.005–0.03 GW/cm² @1064 nm and

*ypchen@sjtu.edu.cn

†These authors contributed equally to this article.

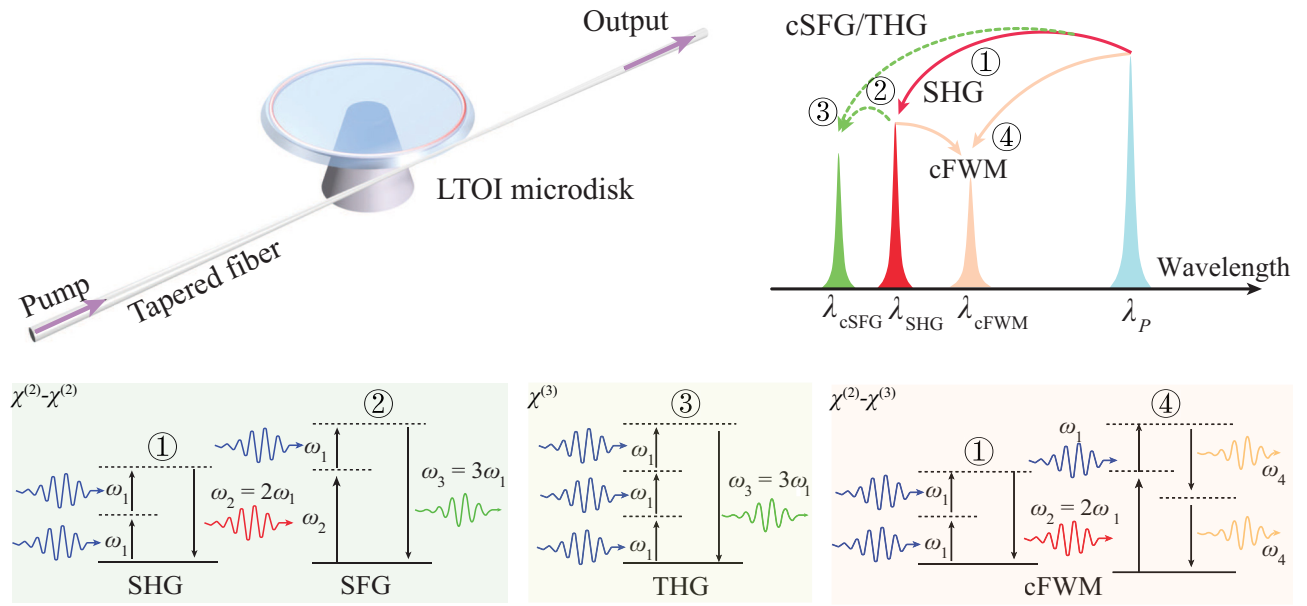


FIG. 1. Schematic of the multiple nonlinear processes generated in the LTOI microdisk and corresponding energy-level diagrams. SHG, second-harmonic generation; cSFG, cascaded sum-frequency generation; THG, third-harmonic generation; cFWM, cascaded four-wave mixing.

10 ns), and UV band opacity (0.4–5.5 μm) [49], which limits its application in high-power light-input conditions, especially for multinonlinear processes in ultrahigh Q microcavities and the mid-UV [50,51].

Lithium tantalate (LT) as one of the key nonlinear nanophotonic platforms has analogous physical properties to LN. Moreover, comparing to the LN, LT has a higher laser-radiation-induced damage threshold (0.22 GW/cm^2 @1060 nm and 30 ns), higher photorefractive damage threshold, and a wider UV transparency (0.28–5.5 μm) [49]. What is more, the LT can withstand large input power, which is beneficial to get more efficient multiple nonlinear optical processes. There is also much research work about the LT based on its similar physical properties to LN such as proton exchange and femtosecond laser direct writing waveguides [52,53], periodically poled lithium tantalate (PPLT), and nonlinear frequency generation [54–61], entangled photons [62], holographic storage [63], strong coupling resonator [64], microwave communication [65], surface acoustic wave (SAW) resonators, and modulators [66,67], etc. Considering the excellent optical nonlinearity of LTOI, it may pave the way to achieve an on-chip wide range of wavelengths coverage via direct optical transition, which is generally considered challenging.

However, most of this research is based on LT bulk materials. The structure is very large and difficult to integrate. In this work, we fabricated high- Q -factor microdisk resonators based on LTOI by optimizing fabrication processes. On-chip near-infrared, visible (red, green) originating from cascade three-wave and four-wave mixing,

were obtained simultaneously. The mode phase-matching conditions of these nonlinear optical processes and SH conversion efficiency were analyzed in detail. The main nonlinear optical processes generated in our LTOI microdisk resonators are shown in Fig. 1. Our work shows a way to use on-chip nonlinear photonics based on LTOI to access interested wavelengths in the near-infrared, visible, and other interested wavelength.

II. DEVICE FABRICATION AND MEASUREMENT

The device, 50- μm -diameter microdisk resonator, is fabricated on a Z-cut LTOI wafer, which has a sandwich structure, from top to bottom as 600-nm-thickness LT crystal, 2- μm -thickness silica, and 500- μm -thickness silicon substrate (prepared by NanoLN Inc.). The main fabrication processes are as follows: First, the disk periphery is milled precisely at the corner edges of LTOI (for better coupling) by using the focused ion beam (FIB) and SEM dual beam system (ZEISS Auriga). To achieve a smoother sidewall of the microdisk resonators, we optimized the current and dose of the ion beam. In order to remove the residual LT crystal from the edge of the microdisk, a microring scanning pattern was used with a smaller current and dose of ion beam.

What is more, after the FIB milling, the sample was slightly polished by chemo-mechanical polishing (CMP) to further smooth the microdisk periphery. At last, the silica layer underneath the LT was partially etched to form the supporting pedestals and support the microdisk, by immersing it in buffered oxide etching (BOE) solution.

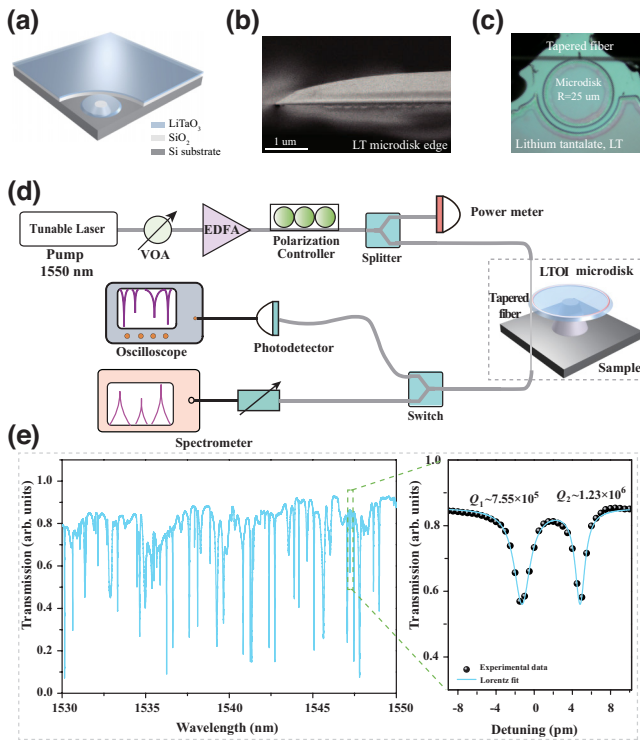


FIG. 2. (a) The schematic LTOI microdisk with silica pedestal, (b),(c) are the SEM image of the LTOI microdisk edge, and optical microscope image (top view) of the whole LTOI microdisk, respectively. (d) Experimental setup: VOA, variable optical attenuator; EDFA, erbium-doped fiber amplifier. (e) The transmission spectrum (1530 to 1560 nm) and Lorentzian fitting of a measured mode are around 1547.23 nm, respectively.

The final shape of the LTOI microdisk is shown schematically in Fig. 2(a). The outermost ring with a perfectly round shape is the boundary of the LTOI microdisk. The inner nearly round border is the boundary of the silica pillar. Figures 2(b) and 2(c) are the SEM of the LTOI microdisk resonator edge and optical microscope image of the whole LTOI microdisk with a tapered fiber from the top view, respectively. It is worth noting that the edge of the microdisk has a smaller wedge angle due to the CMP process [68].

Figure 2(d) schematically shows our experimental setup for characterizing the cascaded three- and four-wave mixing processes. A narrow-linewidth tunable continuous-wave laser [New Focus TLB-6728 (telecom), linewidth < 200 kHz] was used as the pump light source. The pump laser power can be adjusted by a variable optical attenuator (VOA) at a suitable value, then it can be amplified by an erbium-doped fiber amplifier (EDFA). After that, a polarization controller (PC) was used to control the polarization of the input light. Then, it was followed by a 99:1 single-mode fiber splitter for wave splitting. The 1% port is connected to a power meter to monitor the input power in real time. The pump power in the 99% port is

launched into a tapered fiber and coupled into the LTOI microdisk. The tapered fiber, with a waist diameter of approximately $1 \sim 2 \mu\text{m}$, was made by the heating and pulling method and placed on a precise three-dimensional (3D) piezo nano stage. Then we can flexibly change the gap between the tapered fiber and the LTOI microdisk. It is beneficial to optimize the coupling efficiency and make an efficient nonlinear process a reality. The LTOI microdisk was monitored by an optical microscope [not shown in Fig. 2(d)] from the top view. The input laser and generated emission from the microdisk were also coupled out by the same tapered fiber, then followed by a switch. One path is connected to an InGaAs photodetector (PD) and an oscilloscope (OSC) to monitor the transmission spectrum. Another path is linked to the optical spectrum analyzer (OSA, Ocean Optics, Inc., Model HR2000, detection range: 200 to 1100 nm) to monitor the generated spectrum.

III. EXPERIMENTAL RESULTS

We first characterized the optical Q factor of LTOI microdisk resonators in the communication band. A small optical power was loaded into the cavity to avoid cavity thermal effects but also keep it enough to measure the transmission spectrum of the device. The transmission spectrum (1530 to 1560 nm) was obtained, shown in Fig. 2(e). The loaded optical Q factors of two WGM modes around 1547.22 nm, are 7.55×10^5 and 1.23×10^6 , respectively. The LTOI microdisk exhibits lower optical losses, after optimizing the fabrication processes.

Then, with the selected pump laser (around 1556.86 nm) power increasing and the optimized coupling condition, the visible signals (red, 778.43 nm, and green 519.03 nm) generation are observed firstly, which originated from the three-wave mixing (SHG), four-wave mixing (THG, cFWM), and cascaded three-wave mixing processes (cSFG). Figure 3(a) shows the visible signals observed by the optical spectrum analyzer at different input powers in the device. What is more, with the pump power increasing, the generated visible signals even became visible to the naked eye. Figure 3(b) shows the optical image of the scattered visible signal generated in the LTOI microdisk with different input pump power.

It is well known that the phase-matching condition is very useful for effective nonlinear processes. Considering our microdisks were fabricated on a 600-nm Z-cut LTOI and there is no periodic polarization domain reversal. The phase matching in the Z-cut LTOI microdisk between the fundamental and higher harmonic modes might be the mode phase matching (MPM). To further analyze these processes, we simulated possible mode profiles of the pump and visible signal in the device, shown in Fig. 3(c), where we use indices n and m to denote radial and azimuthal mode numbers for the TE/TM $_{n,m}$ profiles in the microdisk. The indices n and m can be calculated

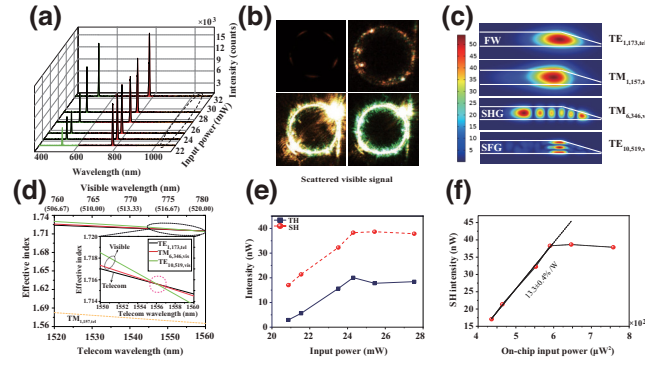


FIG. 3. (a) The recorded spectrum of the visible signal (SHG, cSFG/THG). (b) Optical microscope image of the scattered visible signal with different pump powers (19.89, 23.15, 67.53, 74.14 mW, respectively). (c) Simulated mode profiles of the pump. (d) Effective indices as functions of the wavelength of $TE_{1,173, \text{tel}}$, $TM_{1,157, \text{tel}}$, $TM_{6,346, \text{vis}}$, and $TE_{10,519, \text{vis}}$ in the telecom and visible band, respectively. (e) Generated SH and TH intensity with different input pump power. (f) SHG power versus on-chip pump power square.

based on the simulation and experimental results. The TE modes supported by the Z-cut LTOI microdisk, correspond to the ordinary polarization and the TM modes correspond to the extraordinary polarization. By calculating the effective refractive indices of these corresponding mode profiles, we can find that the MPM was satisfied around 1556 nm, shown in Fig. 3(d), where the inset is a partial enlargement of the $TE_{1,173, \text{tel}}$ (FW in the telecom band), $TM_{6,346, \text{vis}}$ (SHG signal, red, around 778.63 nm), $TE_{10,519, \text{vis}}$ (cSFG signal, green, around 519.03 nm) effective refractive indices, respectively. The effective refractive indices of mode profiles ($TE_{1,173, \text{tel}}$, $TM_{6,346, \text{vis}}$, $TE_{10,519, \text{vis}}$) are very close in the 1556–1560 band, and the closest phase-matching area is around 1556 nm at the temperature of 25°C. That is approximately consistent with our experimental results. It is worth pointing out that only d_{31} was utilized in the $\chi^{(2)}$ -based nonlinear processes of the Z-cut LTOI microdisk, by calculating the effective nonlinear coefficients.

Figure 3(e) shows the generated SH and TH signal intensity with different pump powers. Figure 3(f) shows the SH conversion efficiency is around $13.3 \pm 0.4\%/W$. It is worth noting that, for the simultaneous existence of SHG, THG, and cSFG, there is slight difference in the relationship between the pump power and the SH intensity. Although, in the pump power undepleted condition, we can use quadratic fitting estimation. For the visible signals in these processes, the dynamics of the generated SH and TH modes can be described as follows [69]:

$$\begin{aligned} \frac{dB}{dt} &= \alpha_B B - i\gamma_{21}|A|^2 - i\gamma_{22}|A|C, \\ \frac{dC}{dt} &= \alpha_C C - i\gamma_{31}|A|^3 - i\gamma_{22}|A|B, \end{aligned} \quad (1)$$

where A , B , and C are the fundamental mode, the SH mode and the TH mode, respectively. $\alpha_j = -i\sigma_j - \kappa_j$, $j = A, B, C$, and $\sigma_j = \omega_{j,0} - \omega_j$ is the detuning between the resonant mode and photon frequency. $\kappa_j = \kappa_{j,0} + \kappa_{j,1}$, where $\kappa_{j,0}$ and $\kappa_{j,1}$ are the intrinsic decay rate and the external coupling rate of the corresponding wave, respectively. $\gamma_{21}, \gamma_{22}, \gamma_{31}$ represent the coupling strength of SHG, cSFG, and THG, which depend on the mode-overlapping, momentum-conservation condition, and the geometry of the microcavity, etc. We can solve the intracavity photon amplitude of the SH mode as

$$B = \frac{i\gamma_{21}\alpha_C|A|^2 - \gamma_{22}\gamma_{31}|A|^4}{\alpha_B\alpha_C + \gamma_{22}^2|A|^2}, \quad (2)$$

where $|A|^2 = 2\kappa_{A,1}P_{\text{pump}}/h\omega_A|\alpha_A|^2$, P_{pump} is the pump power and h is the Planck constant. Then, the generated SH power can be obtained as

$$\begin{aligned} P_{\text{SH}} &= 2\kappa_{B,1}h\omega_B|B|^2 \\ &= 2\kappa_{B,1}h\omega_B \left| \frac{i\gamma_{21}\alpha_C|A|^2 - \gamma_{22}\gamma_{31}|A|^4}{\alpha_B\alpha_C + \gamma_{22}^2|A|^2} \right|^2. \end{aligned} \quad (3)$$

Considering the detuning $\sigma_j = 0$, Eq. (3) can be written as

$$\begin{aligned} P_{\text{SH}} &= 2\kappa_{B,1}h\omega_B \\ &\times \frac{4\gamma_{22}^2\gamma_{31}^2\kappa_{A,1}^2P_{\text{pump}}^2/(\kappa_A^4h^2\omega_A^2) + \kappa_C^2\gamma_{21}^2}{(\kappa_B\kappa_C\kappa_A^2h\omega_A/(2\kappa_{A,1}P_{\text{pump}}) + \gamma_{22}^2)^2}. \end{aligned} \quad (4)$$

From Eq. (4) we can find that the power relationship between the fundamental wave and SH is no longer the quadratic equation. Of course, we can still use the quadratic equation to analyze the SHG processes under low pump power and weak TH generation. Also, we can know that, for stronger SH intensity, we need to design the microcavity (geometry, dispersion, phase-matching conditions) carefully to suppress the direct TH and the cSFG processes.

What is more, accompany with the visible signal generation, a weak near-infrared signal was also generated [shown in Fig. 3(a) black dotted ellipse]. We kept increasing pump power and achieved stronger near-infrared signal. Figure 4(a) shows the recorded spectrum under the input pump power at 36.19 mW, with the near-infrared signal (red dotted circle and inset, around 1037.75 nm). Figure 4(b) shows the power dependence of the near-infrared signal on the different pumps in the telecom band, by keeping increasing the input power to around 78.89 mW. The wavelength of the generated near-infrared signal fluctuated slightly with the pump power increasing that may be caused by the thermal effect and photorefractive effect under the high input power condition. By analyzing the photon energy-conservation condition, we found that

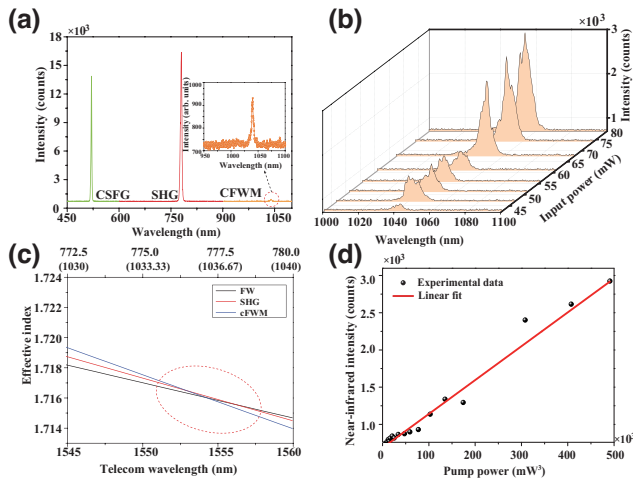


FIG. 4. (a) The recorded spectrum of the visible signal (SHG, cSFG/THG, and cFWM) signal with 36.19-mW pump power. (b) cFWM near-infrared signal generation with different input power. (c) Effective indices as functions of wavelength in the telecom (FW), visible (SHG), and near-infrared (cFWM). (d) The near-infrared SHG signal intensity with the pump-power cubic.

$\omega_A + \omega_B = 2\omega_{\text{NIF}}$, where ω_{NIF} is the frequency of the near-infrared signal. Then we further calculated the effective refractive indices of the input pump wave (FW), its SH signal (SHG), and the generated near-infrared signal (cFWM) as shown in Fig. 4(c), respectively. It shows that the mode phase matching was nearly satisfied too. That means the near-infrared signal originated from a cFWM nonlinear process in the LTOI microdisk resonator, which is a $\chi^{(2)}$ - $\chi^{(3)}$ nonlinear optical process. And, the cFWM process was degenerate. Figure 4(d) shows the near-infrared signal intensity upon the different pump power. The cubic relationship between the near-infrared signal and the pump power is also in agreement with the experimental data.

It is worth mentioning that the cFWM in the visible band is usually neglected due to the infrared band pump light and the low Q of visible modes in the microcavity [70]. Generally speaking, the efficiency of the third-order nonlinear process is very low, especially for the very weak $\chi^{(3)}$ susceptibilities. However, we can use the high- Q microresonator and large pump power to achieve the $\chi^{(3)}$ -based nonlinear processes. Although the conversion efficiency was relatively low, one may design the dispersion, mode overlap area, and domain structure carefully and improve the Q factor to obtain high conversion efficiency. Of course, for these multiple nonlinear processes, more factors may need to be considered, and more research is needed to achieve high conversion efficiency, especially the interference effect among multinonlinear optical processes generation simultaneously [69].

IV. CONCLUSIONS AND DISCUSSION

In conclusion, we fabricated 50- μm -diameter microdisk resonators on a Z-cut LTOI, which have high Q factors (10^6) in the telecom band by optimizing the fabrication, which can significantly enhance the intensity of the intracavity light field. With the loaded pump power increasing, the telecom band, the near-infrared, and visible (red, green) light are also simultaneously achieved, which originated from the three-wave, cascaded three-wave, and four-wave mixing processes. $\chi^{(2)}$ - $\chi^{(2)}$ and $\chi^{(2)}$ - $\chi^{(3)}$ -based nonlinear frequency generation has been realized simultaneously in an LTOI microresonator. The SHG intensity and conversion efficiency were analyzed, and one can improve the efficiency by optimizing the microcavity geometry, pump wavelength, power, phase-matching conditions, etc. And more optical nonlinear processes, for example, optical parametric oscillators (OPOs) and difference frequency generation (DFG), can be generated by designing periodically poled domain structures and the device dispersion in the LTOI microdisk. More broad spectral span frequency combs and even UV signals may also be achieved by careful dispersion design combining the relatively high damage threshold of LTOI microresonators. All these nonlinear process generations in the LTOI microdisk show the great application potential for LTOI in integrated nonlinear photonics. And its outstanding physical properties make it can be an excellent nonlinear photonics and hybrid photonics platform.

ACKNOWLEDGMENTS

This work was supported by the National Natural Science Foundation of China (Grant No. 12134009), the National Key R & D Program of China (Grant No. 2019YFB2203501), Shanghai Municipal Science and Technology Major Project (2019SHZDZX01-ZX06), and SJTU No. 21X010200828.

- [1] J. Y. Chen, C. Tang, Z. H. Ma, Z. Li, Y. M. Sua, and Y. P. Huang, Efficient and highly tunable second-harmonic generation in z-cut periodically poled lithium niobate nanowaveguides, *Opt. Lett.* **45**, 3789 (2020).
- [2] R. Luo, Y. He, H. Liang, M. Li, and Q. Lin, Highly tunable efficient second-harmonic generation in a lithium niobate nanophotonic waveguide, *Optica* **5**, 1006 (2018).
- [3] Y. Zhao, J. K. Jang, Y. Okawachi, and A. L. Gaeta, Theory of $\chi^{(2)}$ -microresonator-based frequency conversion, *Opt. Lett.* **46**, 5393 (2021).
- [4] C. Q. Xu and B. Chen, Cascaded wavelength conversions based on sum-frequency generation and difference-frequency generation, *Opt. Lett.* **29**, 292 (2004).
- [5] L. Ledezma, R. Sekine, Q. Guo, R. Nehra, S. Jahani, and A. Marandi, Intense optical parametric amplification in dispersion-engineered nanophotonic lithium niobate waveguides, *Optica* **9**, 303 (2022).

- [6] C. Wang, C. Langrock, A. Marandi, M. Jankowski, M. Zhang, B. Desiatov, M. M. Fejer, and M. Lončar, Ultrahigh-efficiency wavelength conversion in nanophotonic periodically poled lithium niobate waveguides, *Optica* **5**, 1438 (2018).
- [7] D. N. Puzyrev, V. V. Pankratov, A. Villois, and D. V. Skryabin, Bright-soliton frequency combs and dressed states in $\chi^{(2)}$ microresonators, *Phys. Rev. A* **104**, 013520 (2021).
- [8] J. Q. Wang, Y. H. Yang, M. Li, X. X. Hu, J. B. Surya, X. B. Xu, C. H. Dong, G. C. Guo, H. X. Tang, and C. L. Zou, Efficient frequency conversion in a degenerate $\chi^{(2)}$ microresonator, *Phys. Rev. Lett.* **126**, 133601 (2021).
- [9] R. W. Boyd, *Nonlinear Optics* (Academic Press, New York, 2020).
- [10] K. J. Vahala, Optical microcavities, *Nature* **424**, 839 (2003).
- [11] J. h. Chen, X. Shen, S.-J. Tang, Q. T. Cao, Q. Gong, and Y. F. Xiao, Microcavity nonlinear optics with an organically functionalized surface, *Phys. Rev. Lett.* **123**, 173902 (2019).
- [12] P. J. Zhang, Q. X. Ji, Q. T. Cao, H. Wang, W. Liu, Q. Gong, and Y. F. Xiao, Single-mode characteristic of a supermode microcavity Raman laser, *Proc. Natl. Acad. Sci.* **118**, e2101605118 (2021).
- [13] L. Yao, P. Liu, H. J. Chen, Q. Gong, Q. F. Yang, and Y.-F. Xiao, Soliton microwave oscillators using oversized billion q optical microresonators, *Optica* **9**, 561 (2022).
- [14] J. Liu, F. Bo, L. Chang, C. H. Dong, X. Ou, B. Regan, X. Shen, Q. Song, B. Yao, W. Zhang, Chang-Ling Zou, and Yun-Feng Xiao, Emerging material platforms for integrated microcavity photonics, *Sci. China Phys., Mech. Astron.* **65**, 104201 (2022).
- [15] Y. Y. Li, Q. T. Cao, J. h. Chen, X. C. Yu, and Y. F. Xiao, Microcavity sensor enhanced by spontaneous chiral symmetry breaking, *Phys. Rev. Appl.* **16**, 044016 (2021).
- [16] X. C. Yu, S. J. Tang, W. Liu, Y. Xu, Q. Gong, Y. L. Chen, and Y. F. Xiao, Single-molecule optofluidic microsensors with interface whispering gallery modes, *Proc. Natl. Acad. Sci.* **119**, e2108678119 (2022).
- [17] D. Xu, Z.-Z. Han, Y. K. Lu, Q. Gong, C. W. Qiu, G. Chen, and Y. F. Xiao, Synchronization and temporal nonreciprocity of optical microresonators via spontaneous symmetry breaking, *Adv. Photonics* **1**, 046002 (2019).
- [18] J. C. Shi, Q. X. Ji, Q. T. Cao, Y. Yu, W. Liu, Q. Gong, and Y. F. Xiao, Vibrational Kerr solitons in an optomechanical microresonator, *Phys. Rev. Lett.* **128**, 073901 (2022).
- [19] J. Lu, J. B. Surya, X. Liu, A. W. Bruch, Z. Gong, Y. Xu, and H. X. Tang, Periodically poled thin-film lithium niobate microring resonators with a second-harmonic generation efficiency of 250 000%/w, *Optica* **6**, 1455 (2019).
- [20] I. Breunig, Three-wave mixing in whispering gallery resonators, *Laser Photon. Rev.* **10**, 569 (2016).
- [21] R. Zhuang, J. He, Y. Qi, and Y. Li, High-q thin-film lithium niobate microrings fabricated with wet etching, *Adv. Mater.* **35**, 2208113 (2023).
- [22] C. Wang, M. Zhang, X. Chen, M. Bertrand, A. Shams Ansari, S. Chandrasekhar, P. Winzer, and M. Lončar, Integrated lithium niobate electro-optic modulators operating at CMOS-compatible voltages, *Nature* **562**, 101 (2018).
- [23] M. He, M. Xu, Y. Ren, J. Jian, Z. Ruan, Y. Xu, S. Gao, S. Sun, X. Wen, L. Zhou, Lin Liu, Changjian Guo, Hui Chen, Siyuan Yu, and Liu Liu, and Xinlun Cai, High-performance hybrid silicon and lithium niobate Mach-Zehnder modulators for 100 gbit s⁻¹ and beyond, *Nat. Photonics* **13**, 359 (2019).
- [24] Z. Wang, G. Chen, Z. Ruan, R. Gan, P. Huang, Z. Zheng, L. Lu, J. Li, C. Guo, K. Chen, and Liu Liu, Silicon-lithium niobate hybrid intensity and coherent modulators using a periodic capacitively loaded traveling-wave electrode, *ACS Photonics* **9**, 2668 (2022).
- [25] M. Xu, M. He, H. Zhang, J. Jian, Y. Pan, X. Liu, L. Chen, X. Meng, H. Chen, Z. Li, Xi Xiao, Shaohua Yu, Siyuan Yu, and Xinlun Cai, High-performance coherent optical modulators based on thin-film lithium niobate platform, *Nat. Commun.* **11**, 3911 (2020).
- [26] C. Wang, M. Zhang, M. Yu, R. Zhu, H. Hu, and M. Loncar, Monolithic lithium niobate photonic circuits for Kerr frequency comb generation and modulation, *Nat. Commun.* **10**, 978 (2019).
- [27] M. Zhang, B. Buscaino, C. Wang, A. Shams-Ansari, C. Reimer, R. Zhu, J. M. Kahn, and M. Lončar, Broadband electro-optic frequency comb generation in a lithium niobate microring resonator, *Nature* **568**, 373 (2019).
- [28] Z. Hao, J. Wang, S. Ma, W. Mao, F. Bo, F. Gao, G. Zhang, and J. Xu, Sum-frequency generation in on-chip lithium niobate microdisk resonators, *Photonics Res.* **5**, 623 (2017).
- [29] J. Lin, N. Yao, Z. Hao, J. Zhang, W. Mao, M. Wang, W. Chu, R. Wu, Z. Fang, L. Qiao, Wei Fang, Fang Bo, and Ya Cheng, Broadband quasi-phase-matched harmonic generation in an on-chip monocrystalline lithium niobate microdisk resonator, *Phys. Rev. Lett.* **122**, 173903 (2019).
- [30] L. Ge, Y. Chen, H. Jiang, G. Li, B. Zhu, and X. Chen, Broadband quasi-phase matching in a MgO:PPLN thin film, *Photonics Res.* **6**, 954 (2018).
- [31] S. Liu, Y. Zheng, and X. Chen, Cascading second-order nonlinear processes in a lithium niobate-on-insulator microdisk, *Opt. Lett.* **42**, 3626 (2017).
- [32] R. Luo, Y. He, H. Liang, M. Li, J. Ling, and Q. Lin, Optical parametric generation in a lithium niobate microring with modal phase matching, *Phys. Rev. Appl.* **11**, 034026 (2019).
- [33] H. Jiang, H. Liang, R. Luo, X. Chen, Y. Chen, and Q. Lin, Nonlinear frequency conversion in one dimensional lithium niobate photonic crystal nanocavities, *Appl. Phys. Lett.* **113**, 021104 (2018).
- [34] Z. Hao, L. Zhang, J. Wang, F. Bo, F. Gao, G. Zhang, and J. Xu, Sum-frequency generation of a laser and its background in an on-chip lithium-niobate microdisk, *Chin. Opt. Lett.* **20**, 111902 (2022).
- [35] F. Ye, Y. Yu, X. Xi, and X. Sun, Second-harmonic generation in etchless lithium niobate nanophotonic waveguides with bound states in the continuum, *Laser Photon. Rev.* **16**, 2100429 (2022).
- [36] J. Y. Chen, Z.-H. Ma, Y. M. Sua, Z. Li, C. Tang, and Y. P. Huang, Ultra-efficient frequency conversion in quasi-phase-matched lithium niobate microrings, *Optica* **6**, 1244 (2019).

- [37] N. Amiune, D. N. Puzyrev, V. V. Pankratov, D. V. Skryabin, K. Buse, and I. Breunig, Optical-parametric-oscillation-based $\chi^{(2)}$ frequency comb in a lithium niobate microresonator, *Opt. Express* **29**, 41378 (2021).
- [38] J. Fan, J. Zhao, L. Shi, N. Xiao, and M. Hu, Two-channel, dual-beam-mode, wavelength-tunable femtosecond optical parametric oscillator, *Adv. Photonics* **2**, 045001 (2020).
- [39] H. Jin, F. M. Liu, P. Xu, J. L. Xia, M. L. Zhong, Y. Yuan, J. W. Zhou, Y. X. Gong, W. Wang, and S. N. Zhu, On-chip generation and manipulation of entangled photons based on reconfigurable lithium-niobate waveguide circuits, *Phys. Rev. Lett.* **113**, 103601 (2014).
- [40] Y. Li, Z. Huang, W. Qiu, J. Dong, H. Guan, and H. Lu, Recent progress of second harmonic generation based on thin film lithium niobate, *Chin. Opt. Lett.* **19**, 060012 (2021).
- [41] Y. Liu, X. Yan, J. Wu, B. Zhu, Y. Chen, and X. Chen, On-chip erbium-doped lithium niobate microcavity laser, *Sci. China Phys., Mech. Astron.* **64**, 234262 (2021).
- [42] Z. Chen, Q. Xu, K. Zhang, W.-H. Wong, D.-L. Zhang, E. Y.-B. Pun, and C. Wang, Efficient erbium-doped thin-film lithium niobate waveguide amplifiers, *Opt. Lett.* **46**, 1161 (2021).
- [43] X. Liu, X. Yan, H. Li, Y. Chen, and X. Chen, Tunable single-mode laser on thin film lithium niobate, *Opt. Lett.* **46**, 5505 (2021).
- [44] J. Zhou, Y. Liang, Z. Liu, W. Chu, H. Zhang, D. Yin, Z. Fang, R. Wu, J. Zhang, W. Chen, Zhe Wang, Yuan Zhou, Min Wang, and Ya Cheng, On-chip integrated waveguide amplifiers on erbium-doped thin-film lithium niobate on insulator, *Laser Photon. Rev.* **15**, 2100030 (2021).
- [45] Q. Luo, C. Yang, R. Zhang, Z. Hao, D. Zheng, H. Liu, X. Yu, F. Gao, F. Bo, Y. Kong, Guoquan Zhang, and Jingjun Xu, On-chip erbium-doped lithium niobate microring lasers, *Opt. Lett.* **46**, 3275 (2021).
- [46] M. Cai, K. Wu, J. Xiang, Z. Xiao, T. Li, C. Li, and J. Chen, Erbium-doped lithium niobate thin film waveguide amplifier with 16 dB internal net gain, *IEEE J. Sel. Top. Quantum Electron.* **28**, 1 (2021).
- [47] Y. Chen, Photonic integration on rare earth ion-doped thin-film lithium niobate, *Sci. China Phys. Mech. Astron.* **65**, 294231 (2022).
- [48] Q. Luo, C. Yang, Z. Hao, R. Zhang, D. Zheng, F. Bo, Y. Kong, G. Zhang, and J. Xu, On-chip erbium-doped lithium niobate waveguide amplifiers, *Chin. Opt. Lett.* **19**, 060008 (2021).
- [49] D. N. Nikogosyan, *Nonlinear Optical Crystals: a Complete Survey* (Springer Science & Business Media, New York, 2006).
- [50] K. Moutzouris, G. Hloupis, I. Stavrakas, D. Triantis, and M.-H. Chou, Temperature-dependent visible to near-infrared optical properties of 8 mol% mg-doped lithium tantalate, *Opt. Mater. Express* **1**, 458 (2011).
- [51] L. Wang, X. Zhang, L. Li, Q. Lu, C. Romero, J. R. V. de Aldana, and F. Chen, Second harmonic generation of femtosecond laser written depressed cladding waveguides in periodically poled MgO: LiTaO₃ crystal, *Opt. Express* **27**, 2101 (2019).
- [52] P. J. Matthews and A. R. Mickelson, Instabilities in annealed proton exchange waveguides in lithium tantalate, *J. Appl. Phys.* **71**, 5310 (1992).
- [53] B. Wu, B. Zhang, W. Liu, Q. Lu, L. Wang, and F. Chen, Recoverable and rewritable waveguide beam splitters fabricated by tailored femtosecond laser writing of lithium tantalate crystal, *Opt. Laser Technol.* **145**, 107500 (2022).
- [54] S. C. Kumar and M. Ebrahim-Zadeh, Green-pumped optical parametric oscillator based on fan-out grating periodically-poled MgO-doped congruent LiTaO₃, *Opt. Lett.* **44**, 5796 (2019).
- [55] Y. Liu, Z. Xie, W. Ling, Y. Yuan, X. Lv, J. Lu, X. Hu, G. Zhao, and S. Zhu, Efficiency-enhanced optical parametric down conversion for mid-infrared generation on a tandem periodically poled MgO-doped stoichiometric lithium tantalate chip, *Opt. Express* **19**, 17500 (2011).
- [56] J. P. Meyn and M. Fejer, Tunable ultraviolet radiation by second-harmonic generation in periodically poled lithium tantalate, *Opt. Lett.* **22**, 1214 (1997).
- [57] V. Y. Shur, A. R. Akhmatkhanov, M. A. Chuvakova, A. A. Esin, O. L. Antipov, A. A. Boyko, and D. B. Kolker, in *The European Conference on Lasers and Electro-Optics* (Optica Publishing Group, Munich Germany, 2019), p. ce_p_36.
- [58] S. V. Tovstonog, S. Kurimura, and K. Kitamura, High power continuous-wave green light generation by quasiphase matching in Mg stoichiometric lithium tantalate, *Appl. Phys. Lett.* **90**, 051115 (2007).
- [59] Z. Yellas, M. W. Lee, R. Kremer, K.-H. Chang, M. R. Beghoul, L.-H. Peng, and A. Boudrioua, Multiwavelength generation from multi-nonlinear optical process in a 2D PPLT, *Opt. Express* **25**, 30253 (2017).
- [60] P. Xu, S. H. Ji, S. N. Zhu, X. Q. Yu, J. Sun, H. T. Wang, J. L. He, Y. Y. Zhu, and N. B. Ming, Conical second harmonic generation in a two-dimensional $\chi^{(2)}$ photonic crystal: A hexagonally poled LiTaO₃ crystal, *Phys. Rev. Lett.* **93**, 133904 (2004).
- [61] S. N. Zhu, Y. Y. Zhu, and N. B. Ming, Quasi-phase-matched third-harmonic generation in a quasi-periodic optical superlattice, *Science* **278**, 843 (1997).
- [62] H. Leng, X. Yu, Y. Gong, P. Xu, Z. Xie, H. Jin, C. Zhang, and S. Zhu, On-chip steering of entangled photons in nonlinear photonic crystals, *Nat. Commun.* **2**, 429 (2011).
- [63] J. Imbrock, S. Wevering, K. Buse, and E. Krätzig, Non-volatile holographic storage in photorefractive lithium tantalate crystals with laser pulses, *J. Opt. Soc. Am. B* **16**, 1392 (1999).
- [64] M. Soltani, V. Ilchenko, A. Matsko, A. Savchenkov, J. Schlafer, C. Ryan, and L. Maleki, Ultrahigh Q whispering gallery mode electro-optic resonators on a silicon photonic chip, *Opt. Lett.* **41**, 4375 (2016).
- [65] M. Jacob, J. Hartnett, J. Mazierska, J. Krupka, and M. Tobar, in *TENCON 2003. Conference on Convergent Technologies for Asia-Pacific Region*, Vol. 4 (IEEE, Bangalore, India, 2003), p. 1362.
- [66] J. Koskela, J. V. Knuutila, T. Makkonen, V. P. Plessky, and M. M. Salomaa, Acoustic loss mechanisms in leaky saw resonators on lithium tantalate, *IEEE Trans. Ultrason. Ferroelectr. Freq. Control* **48**, 1517 (2001).
- [67] R. Denton, F. Chen, and A. Ballman, Lithium tantalate light modulators, *J. Appl. Phys.* **38**, 1611 (1967).
- [68] J. Zhang, Z. Fang, J. Lin, J. Zhou, M. Wang, R. Wu, R. Gao, and Y. Cheng, Fabrication of crystalline microresonators

- of high quality factors with a controllable wedge angle on lithium niobate on insulator, [Nanomaterials](#) **9**, 1218 (2019).
- [69] M. Li, C. L. Zou, C. H. Dong, and D. X. Dai, Optimal third-harmonic generation in an optical microcavity with $\chi^{(2)}$ and $\chi^{(3)}$ nonlinearities, [Opt. Express](#) **26**, 27294 (2018).
- [70] M. Li, C. L. Zou, C. H. Dong, X. F. Ren, and D. X. Dai, Enhancement of second-harmonic generation based on the cascaded second-and third-order nonlinear processes in a multimode optical microcavity, [Phys. Rev. A](#) **98**, 013854 (2018).